Colouration by Total Internal Reflection and Interference at Microscale Concave Interfaces

Amy E. Goodling[1†], Sara Nagelberg[2†], Bryan Kaehr[3], Caleb H. Meredith[1], Seong Ik Cheon[4], Ashley P. Saunders[4], Mathias Kolle[2], Lauren D. Zarzar[4]*

1. Department of Materials Science and Engineering, The Pennsylvania State University, University Park, Pennsylvania 16802, USA
2. Department of Mechanical Engineering, Massachusetts Institute of Technology, Cambridge, Massachusetts 02139, USA
3. Advanced Materials Laboratory, Sandia National Laboratories, Albuquerque, NM 87106, USA
4. Department of Chemistry, The Pennsylvania State University, University Park, Pennsylvania 16802, USA

† These authors contributed equally to this work

A variety of physical phenomena create colour: pigments and dyes for spectrally selective light absorption[1,2], material-specific optical dispersion[3] and structural colour by the interference of light[4–11] in micro- and nano-scale periodic structures[12–17]. In addition, there are scattering, diffraction, and interference mechanisms inherent to spherical droplets[18] which induce atmospheric phenomena such as glories, coronas, and rainbows[19]. Here, we describe a previously unrecognized mechanism for creating iridescent structural colour with large angular spectral separation. Light traveling by different trajectories of total internal reflection along a concave optical interface can interfere to generate brilliant patterns of colour. The effect is generated at interfaces with dimensions that are orders of magnitude larger than the wavelength of visible light and is readily observed in systems as simple as water drops condensed on a transparent substrate. We also exploit this phenomenon in complex systems, including multiphase droplets, 3D patterned polymer surfaces, and solid micro-particles, to create patterns of iridescent colour that are consistent with theoretical predictions. Given the ease by which controllable structural coloration is generated at microscale interfaces, we expect that the design principles and predictive theory outlined here will be of interest for fundamental exploration in optics and application in functional colloidal inks and paints, displays, and sensors.

We first observed the structural coloration within monodisperse, biphasic Janus oil droplets containing heptane (refractive index $n_H \approx 1.37$) and perfluorohexane ($n_F \approx 1.27$) dispersed in aqueous surfactant (Figure 1a, see Methods for determination of refractive indices). Upon illumination with collimated white light from above, droplets with an upward facing concave internal interface between the constituent oils exhibit intense angle-dependent coloration in reflection (Figure 1b, Supplementary Video 1). Microscopic observations reveal that the reflected light emanates from a ring near the droplets' three-phase contact line (Figure 1c), suggesting that the color is due to light-matter interactions within single droplets rather than periodic droplet arrangement. Polydisperse droplets of identical oil volume ratios and contact angles were found to exhibit size-dependent color (Figure 1d); the resulting mix of colors gives rise to a glittery white appearance as seen by the unaided eye (Figure 1e). Droplets polymerized into solid particles retain reflected color but do not orient with gravity as well as the liquid droplets, highlighting the importance of the orientation of the hydrocarbon-fluorocarbon interface with respect to the light in generating the optical effect (Figure 1f). As the orientation of the droplet-internal interface was instrumental to the optical mechanism, we wondered whether the colors could be replicated in simpler materials with a similar concave geometry, such as that of a sessile droplet. Upon condensing water onto the underside of a transparent, polystyrene petri dish lid (advancing contact angle, 70°), we observed significant color separation and iridescence (Figure 1g, Supplementary Video 2). Again, the colored light emanates from near the solid-liquid contact line and the effect is dependent on sessile droplet diameter and contact angle (Figure 1h,i). Solid polymeric hemispheres of comparable dimensions to the sessile droplets also show similar behavior (Extended

Data Figure 1), and display varying reflected color when exposed to media of different refractive index (Supplementary Video 3). As a means to systematically quantify the light scattering and iridescence of these materials and capture the entire angular color distribution, we projected the reflected light onto a translucent hemispherical screen (half of a ping-pong ball). This technique allows us to visualize all of the colors for all viewing angles in a single image (Figure 2a-c). We observed that the angular separation of the colors is large, approximately 30-35° from red to blue, for the systems described in Figure 1. This color separation cannot be explained with known structural coloration mechanisms, which are incompatible with the large length scales and geometries of these interfaces. We were thereby motivated to uncover the origin of this iridescence.

Given that the color separation phenomenon is generalizable to microscale concave interfaces with adjacent volumes of high and low refractive index media, and that the light reflects from near the edge of the concave interface, we hypothesized that total internal reflection (TIR) of light along the concave interface plays an important role. However, while TIR explains how light is reflected with pronounced intensity, it alone cannot account for the observed color variations. Material dispersion can also not accurately describe the angular color separation nor the size-dependence in a simple ray-tracing model (Extended Data Figure 2). Consequently, another optical mechanism must be at play. In general, iridescent structural colors are caused by interference of light waves taking different paths through a material[20]. In photonic crystals or gratings, such interference is created through surface or volume periodicity on the order of the wavelength of light, which is not present in our system. Interference of light within spherical water droplets is responsible for the colorful atmospheric effect known as a glory. Typically, optical phenomena caused by scattering spheres, such as glories and rainbows, are modeled using Mie scattering theory[19]. However, Mie theory only applies to particles with spherical symmetry, which is not present in the systems we consider[21]; the sessile droplets and domes are spherical caps and the concave interior interfaces of the biphasic droplets similarly break spherical symmetry. This broken symmetry enables TIR of light along a concave interface, which is not possible in perfect spheres. Hence, we hypothesized that the observed colors result from the interference of this light propagating by TIR on different paths along a concave interface.

To test our prediction, we first considered a simplified system in which light would be expected to propagate in a single plane, such as in a cylindrical segment. Provided the incident light direction is perpendicular to the cylinder symmetry axis, the reflected rays are expected to all lie within the plane perpendicular to that axis (Figure 3a). We used multiphoton lithography to print arrays of cylindrical (Figure 3b,c) and polygonal segments (Extended Data Figure 3) of varying number of sides and observed reflected iridescent color for all structures that supported multiple trajectories of TIR. The interference of light in the cylindrical segments can be theoretically modeled by considering all the different paths that light can take along the interface and accounting for the total phase accumulated along each trajectory (Figure 3d). Thus, we can determine the intensity as a function of wavelength for each light incidence direction and observation angle (Figure 3e). Analytically, this can be expressed as the sum of the complex amplitudes of all light paths that are possible for a given angle of light incidence (θ_{in}) and a fixed observation direction (θ_{out}):

$$I = \left| \sum_{\text{all possible paths}}^{m} A_{\mathrm{m}}(\alpha_{\mathrm{m}}) \cdot r_{\mathrm{m}}\left(\alpha_{\mathrm{m}}, \frac{n_1}{n_2}\right)^{m} \cdot \exp\left(\frac{2\pi i \cdot n_1}{\lambda_0} \cdot l_{\mathrm{m}}(\alpha_{\mathrm{m}})\right) \right|^2 \qquad \text{(Eq. 1)}$$

where the index of summation, m, represents the number of reflections that occur for each trajectory. In the example in Figure 3d, this would be the sum over the three different paths shown, so that m runs from 2 to 4. The local angle of incidence is

$$\alpha_{\mathrm{m}} = \frac{\pi}{2} - \frac{\pi - \theta_{\mathrm{in}} + \theta_{\mathrm{out}}}{2m}. \qquad \text{(Eq. 2)}$$

A_{m} is an amplitude factor, r_{m} is the complex Fresnel reflection coefficient (which effects a phase shift upon each reflection), n_1 and n_2 are the refractive indexes of the medium above and below the interface respectively, and λ_0 is the wavelength of light in air. The phase change due to propagation is captured in the exponential where $l_{\mathrm{m}} = 2mR\cos(\alpha_{\mathrm{m}})$ is the physical path length of each trajectory, with R being the optical interface's radius of curvature. Note that the intensity I is a function of the incident light's wavelength λ_0, the incidence angle θ_{in} and the observation angle θ_{out}. For the detailed derivation, see Supplementary Discussion, "Full derivation of the analytical description of the interference phenomenon in 2D". From the analytically obtained spectral information, we predicted the colors that should be observed (see Supplementary Discussion "Converting spectra into colors") and they matched well with the experimentally determined angular color distribution (Figure 3f,g; Supplementary Discussion "Quantitative angle measurements from the experimentally determined angular color distributions").

We next aimed to predict the scattering behavior of three-dimensional structures. The two-dimensional model was readily extended to treat three-dimensional spherical caps by recognizing that all reflections occur within the plane containing the incoming ray of light and the center of curvature of the spherical interface (Figure 4a). In this plane, we denote the effective light incidence and reflection angles, measured from the spherical cap's in-plane surface normal, as β_{in} and β_{out}. η_{eff} is the effective opening angle. A full derivation of the angles within this plane, in relation to the global coordinates θ_{in}, θ_{out}, φ_{out}, and η as shown in Figure 4a, is given in the Supplementary Discussion, "Extension of the theoretical description to 3D spherical concave optical interfaces". In order to compare results from the model with experiment, we used the biphasic heptane-perfluorohexane droplets but index-matched the aqueous phase to the heptane phase, allowing us to disregard refraction at the droplets' curved upper interface. We found very good agreement between the model and experiment (Figure 4b-h).

We used this three-dimensional model to better understand how various geometrical and material-specific parameters affect the color distribution. The total phase change for a given path, and thus the interference condition, depends on the product $n_1 R$ in the optical path length and the refractive index contrast in the Fresnel coefficient $r_{\mathrm{m}}(\alpha_{\mathrm{m}}, \frac{n_1}{n_2})$. The allowed trajectories for a given $(\theta_{\mathrm{in}}, \theta_{\mathrm{out}})$ are set by the opening angle η as well as illumination and observation directions. Figure 4b-e show how each of these parameters (R, θ_{in}, η, and n_2) affects the colors observed as a function of observation direction θ_{out} for the azimuthal angle $\varphi_{\mathrm{out}} = 180°$. As the radius of curvature R increases, the color patterns shift to larger angles and the spread of colors decreases, as shown in Figure 4b,f and Extended Data Figure 4a). The angular location of the color bands varies almost linearly with the illumination direction, θ_{in}, as seen in Figure 4c,g and Extended Data Figure 4b. This can be understood by interpreting a change in illumination angle θ_{in} as a rotation of all ray paths around the center of curvature of the interface. Once rotated too far, a ray trajectory may no longer be available, which is evident in the sharp changes in color in Figure 4c. The opening angle, η, does not affect the phase of the light; consequently, the locations of the color bands are constant as η is varied (Figure 4d). However, whether a specific trajectory is possible strongly depends on η. Regions of grey indicate that only one possible trajectory exists and thus there is no interference that could lead to color. The effect of the refractive index contrast can be seen by adjusting n_2 (Figure 4e). The sharp changes in color as n_2 decreases correspond to where TIR begins to occur for another trajectory. These transitions are likely smoother than shown here, as we have not included light that is reflected with high amplitude but below the critical angle. These results suggest that we should be able to design specific, desired structural color patterns and fabricate the required surface to generate the predicted iridescence.

A unique aspect of the iridescent biphasic oil droplets is that they can be reconfigured between Janus and double emulsion morphologies by tuning the balance of interfacial tensions[22]. This morphological change allows us to manipulate the curvature of the oil-oil interface where the TIR occurs which should, in turn, influence the reflected color. We varied the droplet morphology between Janus and double emulsion configurations by adjusting surfactant concentrations in the water and observed that the only droplet shapes that reflect light when illuminated from above are those having a partially open and concave curvature between the two oils (e.g. droplets ii-v in Figure 5a). This is consistent with predictions, as only the partially open concave interfaces that transition from high to low refractive index can support multiple paths of TIR leading to interference. Also consistent with the model is the observation that the iridescence produced is exquisitely sensitive to slight changes in the curvature and opening angle of the oil-oil interface where TIR occurs. By introducing a light-responsive azobenzene surfactant, (4-butylphenyl)-2-(4-trimethylammoniumpropoxyphenyl) diazene[22,23], we could use UV and blue light to photo-pattern the droplet morphologies and create reflective colored images (Figure 5b). Such responsive, tunable droplet colors could be of interest for sensors or displays.

We have described a design principle by which to create structural coloration via interference occurring when light undergoes multiple total internal reflections at microscale interfaces. Although this phenomenon has not been previously studied, we find it to be commonplace, as it observed in even simple microscale droplets on transparent surfaces. Key requirements to generate this effect are: 1) a refractive index interfacial contrast that supports total internal reflection, and 2) a microscale geometry that supports multiple trajectories for total internal reflection of light for specific directions of light incidence and observation. We expect this color effect to persist until the optical path length difference of various light trajectories along the interface exceeds the coherence length of the incident light. We have presented a detailed analytical model with predictive capabilities as verified by close matching of experimentally determined and modeled angular color distributions. Our model allows us to rationalize color variations observed for variables such as radius of curvature, contact angle, refractive index contrast, and incident light angle. We leveraged this optical effect to create structural coloration within a wide range of materials and geometries including sessile droplets, biphasic droplets, solid particles, and polymeric microstructures with both curved and flat sides. The design principles laid forth will be of significant interest and use to scientists and engineers from a wide variety of fields who seek to modulate the color and reflective optical properties of materials.

Methods

Chemicals:

All chemicals were used as received. Capstone FS-30 (Dupont); perfluorohexane(s) (98%) and 1H,1H,2H,2H-perfluorodecyl acrylate (97%) (Synquest Laboratories); Triton X-100 (Alfa Aesar); heptane (>99%) (MilliporeSigma); Sartomer CN4002 fluorinated oligomer (Arkema); 2-hydroxy-2-methyl-1-phenylpropan-1-one (97%) (Ark Pharm Inc.); Sylgard 184 polydimethylsiloxane (PDMS) (Dow Corning); Norland Optical Adhesive 61 (Norland); Pluronic F-127 (bioreagent grade), sodium dodecyl sulfate (98%) and trimethylolpropane ethoxylate triacrylate ($M_n \approx 428$ g/mol) (Sigma-Aldrich). The light-responsive azobenzene surfactant, (4-butylphenyl)-2-(4-trimethylammoniumpropoxyphenyl) diazene, was synthesized as described elsewhere[23].

Refractive index measurement of droplet oils:

Heptane and perfluorohexane were mixed in a 1:1 volume ratio at ambient temperature and allowed to phase separate, simulating the fluid conditions inside the biphasic droplets. The two phase-separated oil layers were then extracted and their refractive indices were measured using a J457FC refractometer (Rudolph Research Analytical). The refractive indices of the oils differ from the pure chemicals due to a degree of mutual solubility.

Fabrication of droplets:

Fabrication of monodisperse emulsions was accomplished using a flow focusing four-channel glass hydrophilic microfluidic chip with a 100 µm channel depth (Dolomite). Each inlet microchannel was connected to a reservoir of the desired liquids. The inlets for the inner phase fluids (e.g. heptane and perfluorohexane) were connected to the reservoirs with 0.0025 inch ID, 1/16 inch OD PEEK tubing of 26 inches in length, and the outer phase aqueous surfactant solution was connected to the reservoirs with 0.005 inch ID, 1/16 inch OD PEEK tubing of 26 inches in length. The flow rate of each liquid was controlled by a Fluigent MFCS-EZ pressure controller thus providing the ability to vary the size of the drops and the volume ratios of the liquids in each drop. Typical pressures used for the inner phase fluids ranged from 1000 mbar to 7000 mbar and pressures for the outer phase fluids ranged from 200 mbar to 3000 mbar. Varying ratios of Capstone FS-30 and Triton X-100 surfactants were used to tune the droplet shape via mechanisms described in detail elsewhere[22]. While many concentrations and ratios of surfactants could be used, as an example we often used aqueous solutions of 1.5 wt% Capstone FS-30 and 0.05 wt% Triton X-100 to stabilize a morphology of droplet which produced the iridescence. Additional Capstone FS-30 and Triton X-100 could be added to tune the droplet shape as desired.

Fabrication of particles:

Biphasic droplet emulsions were created through the use of a 4-channel microfluidics apparatus as described in the section “Fabrication of Droplets”. To make particles, monomers were used as the fluids for subsequent polymerization into particles. The hydrocarbon monomer was trimethylolpropane ethoxylate triacrylate with 5 v/v% photoinitiator, 2-hydroxy-2-methyl-1-phenylpropan-1-one. The fluorinated monomer was Sartomer CN4002 fluorinated oligomer mixed with 1H,1H,2H,2H-perfluorodecyl acrylate in a 3:1 volume ratio. 1 wt% Pluronic F-127 in water was used as the continuous phase. PEEK tubing of 2 foot length with 0.005 inch ID and pressures of 500 mbar were used for all four inlet flows. Once the droplets were fabricated, 1 wt% sodium dodecyl sulfate in water was added to the droplet solution until the droplets exhibited a Janus shape that reflected light. Droplets were then polymerized into solid particles by curing under an OmniCure UV lamp (mercury bulb, 17 W/cm^2) for 30 seconds.

Sample imaging:

Microscopic imaging for determining droplet shape: The droplets were imaged using a Nikon Eclipse Ti-U inverted microscope. The droplets naturally orient with the denser fluorocarbon side downward, so to image the droplet profile, the emulsions were shaken in order to induce the droplets to roll onto their side and then the image was captured using a <1 ms exposure with an Image Source DFK 23UX249 color camera. To image droplets in reflection, an upright microscope with a QImaging Micropublisher 3.3 RTV color camera was used.

Macroscopic imaging of droplet color: A monolayer of the emulsion droplets were placed in a petri dish with aqueous surfactant solution. The bottom of the dish was painted with black acrylic paint. For large area illumination, an Amscope LED-50W light with a collimating lens was used to illuminate the sample. For selected area illumination, a Thorlabs LED light (MWWHF2, 4000 K, 16.3 mW) equipped with a Ø200 µm fiber optic cable and collimating lens (CFC-2X-A) was used. The translucent dome used for capturing the iridescent color pattern was created by cutting a 40 mm diameter ping-pong ball in half with a razor blade and drilling a 3 mm diameter hole in the side with a Dremel Model 220. The ping-pong ball dome screen was then placed on the 35 mm petri dish lid containing the emulsion and collimated light from the LED was passed through the hole into the center of the dish. All macroscale photographs were taken using a Canon EOS Rebel T6 DSLR camera mounted to an optical table and positioned at specific angles, as indicated in the primary text.

Reflection from sessile water drops and contact angle:

The advancing contact angle of water on a polystyrene petri dish was measured using a goniometer (ramé-hart). Sessile water drops were imaged in reflection using a Nikon Eclipse Ti-U inverted microscope (for microscopic imaging) or with a Canon EOS Rebel T6 DSLR camera (for macroscopic photographs). The water drops were created by placing warm water in a dish under the room temperature petri dish substrate and allowing water to condense. The macroscale patterned reflectance image of the elephant was created using selected area UV-ozone treatment to increase the hydrophilicity of the polystyrene surface. A laser cutter was used to cut an elephant shape out of paper which was placed over the hydrophobic surface of a polystyrene petri dish to use as a mask during UV-ozone treatment. Unexposed areas of the polystyrene remained hydrophobic, while UV-ozone treated areas were hydrophilic (low contact angle) and no longer supported total internal reflection and hence had no iridescent color.

Fabrication, characterization, and imaging of polymer domes, horizontal cylindrical segments, and polygons

Nanoscribe fabrication. Arrays of solid domes, horizontal cylindrical segments, and polygons were created using the Photonic Professional GT Nanoscribe. This equipment allows the user to three dimensionally print structures using multiphoton near-IR direct laser writing. Structures were printed onto fused silica glass slides with a 60x objective with the resist IP-Dip 65 (*n* = 1.54) or IPS (*n* = 1.51) using a 100 or 200 nm step size. The domes were computationally rendered with 3ds Max software and the cylinders and polygons were rendered with AutoCAD. Both renderings were converted into a DeScribe file format to import into the Nanoscribe. Uncured resist was washed away with AZEBR for 20 minutes and isopropanol for 2 minutes.

Replication of polymer structures. Dow Corning Sylgard 184 PDMS was used to create a replica from the structures printed with the Nanoscribe. The PDMS base and hardener were mixed in a 10:1 mass ratio, mixed, poured over the polymer sample, and cured in an oven at 70°C for at least two hours. The cured PDMS was peeled off of the structures to yield an array of wells. The PDMS mold could then be used to replicate the structures into different refractive index polymers, such as Norland Optical Adhesive (NOA) 61 (*n* = 1.56). After allowing the polymer to fill the PDMS wells, the sample was backed with glass, and the resin was cured using a UV lamp (17 W/cm^2, 20 seconds). The NOA 61 was then peeled out of the PDMS mold to yield an array of replicated structures.

Effect of refractive index contrast. Domes fabricated in NOA 61 (n=1.56) on a glass substrate could be placed in various solvents to observe the effects on refractive index contrast on the color. In Supplementary Video 3, the domes were imaged in reflection using a Nikon Ti-U Eclipse and Image Source DFK 23UX249 color camera. NIS-Elements software was used to record a video of the reflected colors as methanol evaporated off the surface.

Implementation of the theoretical optical model:

The model presented in the primary text was implemented in MATLAB. In the 2D case, the parameters for the radius of curvature of the droplet-internal interface R, the refractive indices n_1 and n_2, the contact angle η, and the light incidence angle θ_{in} were fixed and the following sum was computed for each value of observation angle θ_{out} and light wavelength λ_0:

$$I = \left|\sum_{m_{+\min}}^{m_{+\max}} \sqrt{\frac{\cos(\alpha_{m+})}{m}} \cdot r_+^m \cdot \exp\left(4i\pi n_1 \cdot \frac{R}{\lambda_0} \cdot m \cdot \cos(\alpha_{\mathrm{m}+})\right)\right|^2 + \left|\sum_{m_{-\min}}^{m_{-\max}} \sqrt{\frac{\cos(\alpha_{m-})}{m}} \cdot r_-^m \cdot \exp\left(4i\pi n_1 \cdot \frac{R}{\lambda_0} \cdot m \cdot \cos(\alpha_{\mathrm{m}-})\right)\right|^2$$

with $\alpha_{m\pm} = \frac{\pi}{2} - \frac{\pi \pm (\theta_{\mathrm{out}} - \theta_{\mathrm{in}})}{2m}$, $m_{\pm\min} = \left\lceil \frac{\pi \pm (\theta_{\mathrm{out}} - \theta_{\mathrm{in}})}{\left(\pi - 2\sin^{-1}\left(\frac{n_2}{n_1}\right)\right)} \right\rceil$, and $m_{\pm\max} = \left\lfloor \frac{\pi\pm(\theta_{\text{out}}-\theta_{\text{in}})}{(\pi-2\alpha_{\pm\max})} \right\rfloor$, where $\alpha_{\pm\max} = \min\left(\frac{\pi}{2} - \left|\frac{\pi}{2} - (\eta \pm \theta_{\text{in}})\right|, \frac{\pi}{2} - \left|\frac{\pi}{2} - (\eta \mp \theta_{\text{out}})\right|\right)$ (see Supplementary Discussion for detailed derivations). r_+ and r_- are the Fresnel coefficients, which depend on the refractive index contrast $\frac{n_1}{n_2}$, the light polarization, and α_{m+} and α_{m-} respectively. The two sum-squared terms represent the two different families of light trajectories for light incident and reflected at the same angles on opposing sides of the concave optical interface.

In the model, output spectra were averaged for input illumination angles lying in a cone from -5° to +5° to approximate the small divergence of the light source used in the experiments, and the lamp's spectrum was used for input spectral intensities. The calculated intensity spectrum for each value of θ_{out} can then be converted to CIE xyz color coordinates using the color matching functions[24,25]. The CIE coordinates were then converted to sRGB[26] in order to be displayed.

For three dimensions, the same sum was used but with

$$\alpha_{m\pm} = \frac{\pi}{2} - \frac{\pi\pm(\beta_{\text{out}}-\beta_{\text{in}})}{2m},\ m_{\pm\min} = \left\lceil \frac{\pi\pm(\beta_{\text{out}}-\beta_{\text{in}})}{\left(\pi-2\sin^{-1}\left(\frac{n_2}{n_1}\right)\right)} \right\rceil \text{ and } m_{\max} = \left\lfloor \frac{\pi\pm(\beta_{\text{out}}-\beta_{\text{in}})}{(\pi-2\alpha_{\max})} \right\rfloor,$$

where $\alpha_{\max} = \min\left(\frac{\pi}{2} - \left|\frac{\pi}{2} - (\eta_{\text{eff}} + \beta_{\text{in}})\right|, \frac{\pi}{2} - \left|\frac{\pi}{2} - (\eta_{\text{eff}} - \beta_{\text{out}})\right|\right)$. β_{in}, β_{out}, and η_{eff} are the effective angles in the plane of incidence as shown in Figure 4a. They are related to the global angles by:

$$\cos(\beta_{\text{in}}) = B\cos\theta_{\text{in}}$$
$$\cos(\beta_{\text{out}}) = -B\cos(\theta_{\text{out}})$$
$$\cos(\eta_{\text{eff}}) = B\cos(\eta)$$

with

$$B = \frac{|\sin(\psi)|}{\sqrt{(\sin^2(\psi) - \sin^2(\theta_{\text{in}})\ \sin^2(\theta_{\text{out}})\sin^2(\phi_{\text{out}}))}}.$$

Here, ψ is the angle between the incoming and outgoing ray of light:

$$\cos(\psi) = \sin(\theta_{\text{out}})\sin(\theta_{\text{in}})\cos(\phi_{\text{out}}) + \cos(\theta_{\text{in}})\cos(\theta_{\text{out}})$$

In order to visualize the data in a manner similar to the ping pong ball projections, theoretical angular color distribution maps were created from the calculated intensities $I(\lambda, \theta_{\text{out}}, \phi_{\text{out}})$ and the corresponding sRGB colors. The (x, y) coordinates of the color distribution image (measured from the center) relate to the direction of observation via the equations $x = k\sin(\theta_{\text{out}})\cos(\phi_{\text{out}})$ and $y = k\sin(\theta_{\text{out}})\sin(\phi_{\text{out}})$ where k is an arbitrary scaling factor to set the image size.

Data availability All relevant data generated or analyzed for this study are included in this published article (and its supplementary information files).

Code availability The MATLAB code used to implement the model is available for download from https://github.com/snnagel/Structural-Color-by-Cascading-TIR.

References

1. Dirac, P. A. M. The quantum theory of the emission and absorption of radiation. *Proc. R. Soc. A Math. Phys. Eng. Sci.* **114,** 243–265 (1927).

2. Kuhn, H. A quantum-mechanical theory of light absorption of organic dyes and similar compounds. *J. Chem. Phys.* **17,** 1198–1212 (1949).

3. Southall, J. P. C. *Mirrors, prisms and lenses: a text-book of geometrical optics*. (The Macmillan Company, 1918).

4. Ghiradella, H. Light and color on the wing: structural colors in butterflies and moths. *Appl. Opt.* **30,** 3492 (1991).

5. Tadepalli, S., Slocik, J. M., Gupta, M. K., Naik, R. R. & Singamaneni, S. Bio-optics and bio-inspired optical materials. *Chem. Rev.* **117,** 12705–12763 (2017).

6. Zhao, Y., Xie, Z., Gu, H., Zhu, C. & Gu, Z. Bio-inspired variable structural color materials. *Chem. Soc. Rev.* **41,** 3297 (2012).

7. Land, M. F. The physics and biology of animal reflectors. *Prog. Biophys. Mol. Biol.* **24,** 75–106 (1972).

8. Kinoshita, S. & Yoshioka, S. Structural colors in nature: the role of regularity and irregularity in the structure. *ChemPhysChem* **6,** 1442–1459 (2005).

9. Vignolini, S. *et al.* Pointillist structural color in pollia fruit. *Proc. Natl. Acad. Sci. U. S. A.* **109,** 15712–5 (2012).

10. Fernandes, S. N. *et al.* Structural color and iridescence in transparent sheared cellulosic films. *Macromol. Chem. Phys.* **214,** 25–32 (2013).

11. Whitney, H. M. *et al.* Floral iridescence, produced by diffractive optics, acts as a cue for animal pollinators. *New Ser.* **323,** 130–133 (2009).

12. Kinoshita, S., Yoshioka, S. & Miyazaki, J. Physics of structural colors. *Reports Prog. Phys.* **71,** 076401 (2008).

13. Merritt, E. A spectrophotometric study of certain cases of structural color. *J. Opt. Soc. Am.* **11,** 93 (1925).

14. Loewen, E. G. & Popov, E. *Diffraction gratings and applications*. (CRC Press, 1997).

15. Macleod, H. A. *Thin-film optical filters*. (CRC Press, 2010).

16. Hutley, M. C. Interference (holographic) diffraction gratings. *J. Phys. E.* **9,** 513–520 (1976).

17. Yablonovitch, E. Photonic crystals. *J. Mod. Opt.* **41,** 173–194 (1994).

18. Hulst, H. C. *Light Scattering by Small Particles*. (Courier Corporation, 1981).

19. Nussenzveig, H. M. High-Frequency Scattering by a Transparent Sphere. II. Theory of the Rainbow and the Glory. *J. Math. Phys.* **10,** 125–176 (1969).

20. Born, M. & Wolf, E. *Principles of optics: electromagnetic theory of propagation, interference and diffraction of light*. (Pergamon Press, 1980).

21. Wriedt, T. A Review of Elastic Light Scattering Theories. *Part. Part. Syst. Charact.* **15,** 67–74 (1998).

22. Zarzar, L. D. *et al.* Dynamically reconfigurable complex emulsions via tunable interfacial tensions. *Nature* **518,** 520–4 (2015).

23. Chevallier, E. *et al.* Pumping-out photo-surfactants from an air–water interface using light. *Soft*

Matter **7,** 7866 (2011).

24. Commission Internationale de L'Eclairage. *CIE 015:2004: colorimetry*. (2004).

25. Gupte, V. C. in *Colour measurement : principles, advances and industrial applications* 70–86 (Woodhead Pub, 2010).

26. Burger, W. & Burge, M. J. in *Digital Image Processing* 341–365 (Springer, London, 2016). doi:10.1007/978-1-4471-6684-9_14

27. Polyanskiy, M. N. Refractive index database. Available at: https://refractiveindex.info/. (Accessed: 20th August 2018)

28. Stiles, V. E. & Cady, G. H. Physical properties of perfluoro-n-hexane and perfluoro-2-methylpentane. *J. Am. Chem. Soc.* **74,** 3771–3773 (1952).

Acknowledgments L.D.Z., A.E.G., C.H.M., A.P.S., and S.C. acknowledge support from the Department of Materials Science and Engineering, the Department of Chemistry, and the Materials Research Institute at The Pennsylvania State University. S.N. and M.K. were supported in part by the U. S. Army Research Office through the Institute for Soldier Nanotechnologies at MIT, under Contract Number W911NF-13-D-0001. A.E.G., S.N., M.K., and L.D.Z. gratefully acknowledge support by the National Science Foundation's CBET program on "Particulate and Multiphase Processes" under grant number 1804241. C.H.M. acknowledges support from the Thomas and June Beaver Fellowship and A.P.S. received support from the Office of Science Engagement at Penn State.

Author Contributions A.E.G., S.N., M.K., and L.D.Z. developed the concept for the research. A.E.G. and L.D.Z. conducted experiments involving droplet and surface fabrication, optical imaging, and photography. S.N. and M.K. provided advice on the optical experiments. A.P.S. and L.D.Z fabricated the Janus particles. S.N. and M.K. developed the optical theory and model. C.H.M. conducted experiments with wetted droplets. B.K. fabricated cylindrical and polygonal segment structures with multiphoton lithography. S.C synthesized the light responsive surfactant. All authors contributed to the writing of the manuscript.

Author Information Reprints and permissions information are available at www.nature.com/reprints. The authors declare no competing financial interests. Sandia National Laboratories is a multimission laboratory managed and operated by the National Technology and Engineering Solutions of Sandia, LLC, a wholly owned subsidiary of Honeywell International, Inc. for the U.S. Department of Energy's National Nuclear Security Administration under contract DE-NA0003525. This paper describes objective technical results and analysis. Any subjective views or opinions that might be expressed in this paper do not necessarily represent the view of the U.S. Department of Energy or the United States Government. Correspondence and requests for materials should be addressed to L.D.Z. (ldz4@psu.edu)

Figures

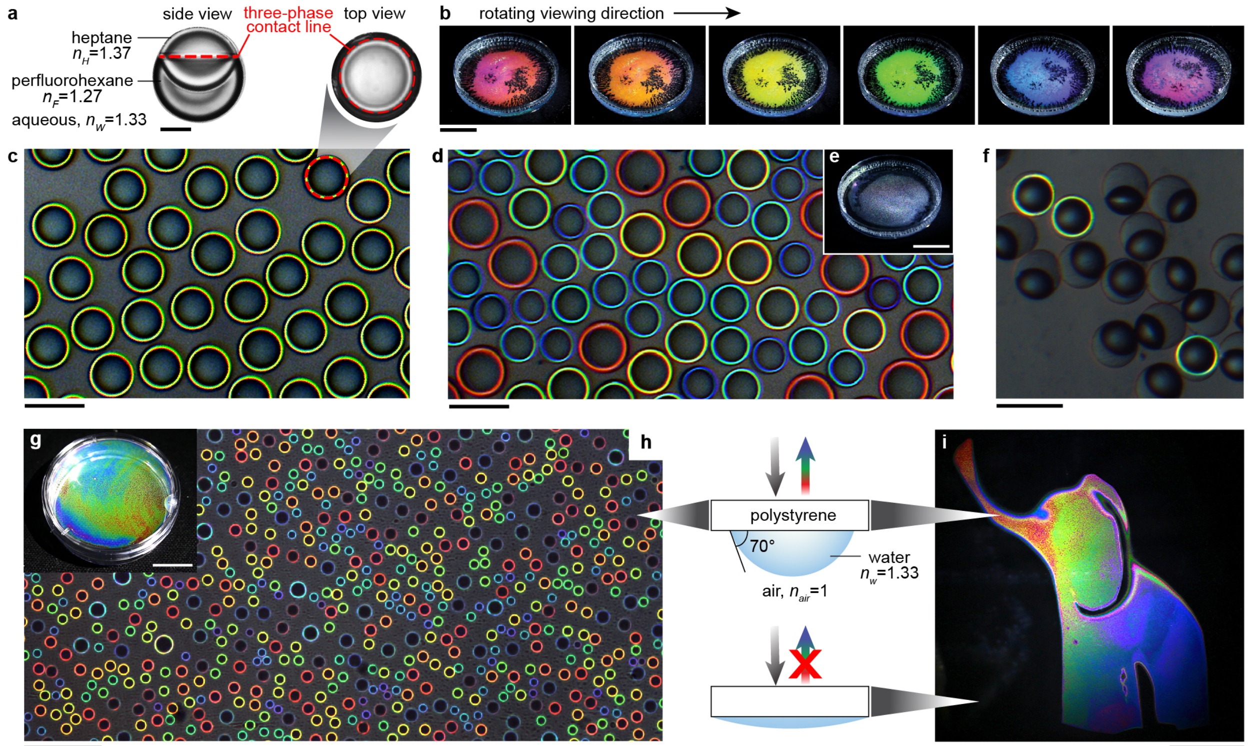

Figure 1 | Microscale concave surfaces display colorful iridescence in reflection. **a**, Schematic and optical micrograph showing the biphasic droplet geometry and composition used in (b-e). The droplets orient with gravity with the denser perfluorohexane side downward, as shown. Scale, 25 µm. **b**, A petri dish containing a monolayer of monodisperse droplets as shown in (a) was illuminated with collimated white light from a fixed direction and photographed at several different observation angles to demonstrate variation in reflected color (Supplementary Video 1). Scale, 2 cm. **c**, Microscopically, each droplet from (b) reflects the same color, irrespective of the location of neighboring drops. The color always emanates from near the three-phase contact line of the droplets. Scale, 100 µm. **d**, Polydisperse droplets all having the same morphology and composition as in (a) but varying size show different colors in reflection. Scale, 100 µm. **e**, Macroscopically, the polydisperse droplets in (d) reflect glittery white light. Scale, 2 cm. **f**, Reflection optical micrograph of solid particles dispersed in water of the same general morphology as shown in (a). Trimethyloylpropane triacrylate ($n \approx 1.56$) was used in place of heptane, Sartomer fluorinated oligomer ($n \approx 1.33$) mixed with 1H,1H,2H,2H-perfluorodecyl acrylate ($n \approx 1.34$) replaced perfluorohexane, and the monomers were polymerized by UV initiation (see Methods). The particles did not orient as uniformly as the liquid droplets, highlighting the importance of the orientation of the hydrocarbon-fluorocarbon interface to enabling reflection. Scale, 100 µm. **g**, Photograph of water droplets condensed onto the underside of a polystyrene petri dish lid illuminated with white light and viewed in reflection (Supplementary Video 2). Scale, 1 cm. **h**, Reflectance optical micrograph of water droplets condensed onto a polystyrene petri dish showing how the color emanates from near the contact line and varies with droplet diameter. Scale, 200 µm. **i**, Reflectance photograph showing the colorful image created when water is condensed onto a polystyrene petri dish with surface hydrophilicity patterned in the shape of an elephant. While there is water condensed over the entire surface, the more hydrophilic UV-ozone treated regions appear black while the untreated regions (contact angle, 70°) have reflected color, demonstrating the importance of the contact angle to generating the optical effect. Scale, 3 cm.

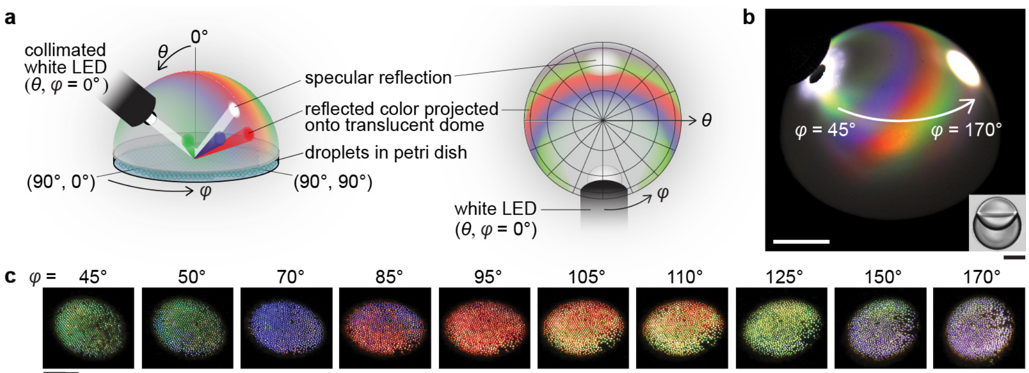

Figure 2 | Biphasic droplet iridescence was mapped in three dimensions for varying droplet size and oil-oil interfacial curvature. a, Side and top view schematics of the experimental setup and coordinate system used to visualize the iridescent color reflected from the droplets in three dimensions. A translucent hemispherical dome screen (half a ping-pong ball) was placed over a petri dish containing monodisperse droplets. Collimated white light from an LED was introduced through a 3 mm hole cut into the side of the domed screen. Colors reflected from the drops projected onto the internal surface of the dome screen. **b**, Side view photograph of an exemplary iridescence pattern (scale, 1 cm) with illumination at θ = 40° and an inset showing the shape of droplets used (scale, 50 µm). **c**, The screen from (b) was removed and the droplets were photographed at different viewing angles under the same illumination angle to demonstrate correlation of the macroscopic colors with the mapped angular position of color onto the screen in (b). Scale, 2 mm.

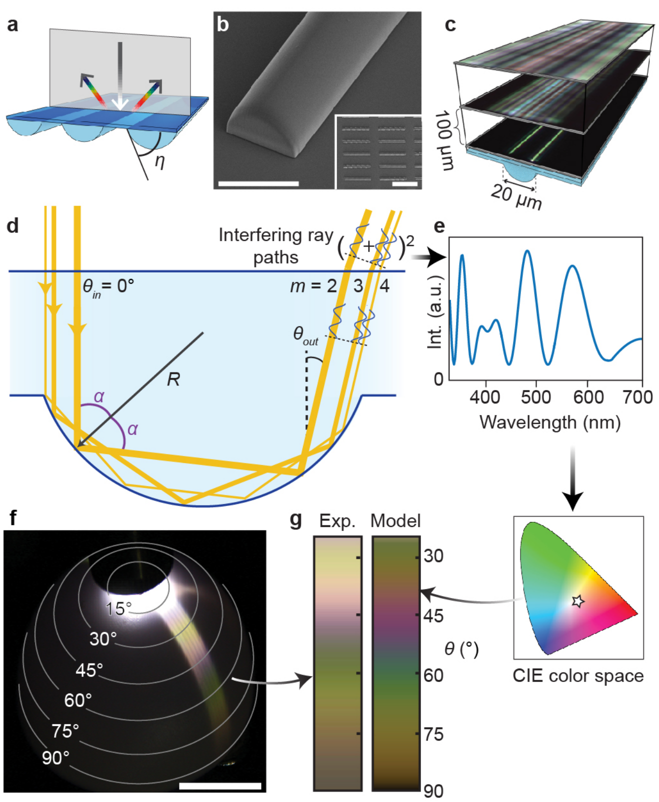

Figure 3 | 2D model of the optical mechanism for structural color generation upon cascading total internal reflections. a, Diagram of horizontal cylindrical segments with η, the contact angle, defined. **b,** Scanning electron micrographs of the horizontal cylindrical segments as fabricated by multiphoton lithography with a radius of curvature of 10.64 µm and a contact angle of 70°. The higher magnification image shows the cylindrical edge (scale, 20 µm) and the lower magnification inset shows a portion of the structure array (scale, 200 µm). **c,** Optical micrographs of a cylindrical segment, in focus and defocused by 100 µm and 200 µm, showing how the reflected color patterns evolve farther from the surface. **d,** Diagram of three rays taking different trajectories along the concave interface that interfere causing the observed coloration. The input and output angles $(\theta_{\text{in}}, \theta_{\text{out}})$ are measured from the global sample surface normal to the left (θ_{out} is negative as shown). **e,** Spectrum derived from Equation 1 for $(\theta_{\text{in}}, \theta_{\text{out}}) = (0°, -13.09°)$ (corresponding to 0° input, -20° output in air). The image below shows the coordinates of this spectrum in the CIE color space. **f,** Reflected color distribution from the horizontal cylindrical segments when illuminated at normal incidence. Lines of constant θ are shown. Scale, 2 cm. **g,** Comparison of color distribution from model and experiment for 0° illumination of the 70° contact angle horizontal cylindrical segments. The input illumination of the calculated colors was averaged over a cone from -5° to +5° in order to approximate the divergence of the light source, and the lamp's spectrum was used for input spectral intensities in the model. The brightness of the experimental dataset was increased by multiplying by a factor of $(1 - 0.8\cos\theta)$ in order to better see the colors at high angles. Low angles were obscured by the specular reflection.

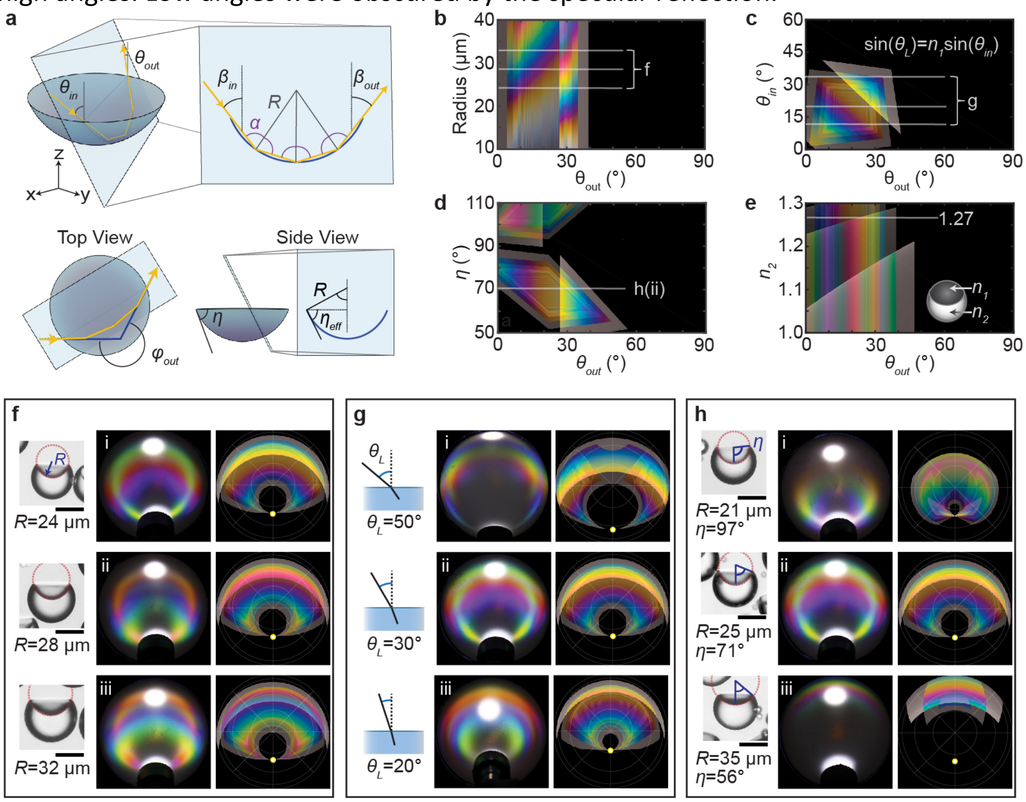

Figure 4 | Extension of model to 3D spherical interfaces and comparison with experiment for index matched Janus droplets. a, Diagram of a light path in a 3D spherical cap. Light is confined to the plane through the center of curvature of the interface and the line defined by the incoming light ray direction. Within this plane, the system can be reduced to two dimensions with effective opening angle, η_{eff}, and effective input and output angles, β_{in} and β_{out}. **b-e,** The color distribution as a function of θ_{out} when changing: **b,** the radius of curvature, **c,** the illumination direction within the medium with refractive index n_1, **d,** the opening angle η, and **e,** the refractive index of the fluorocarbon phase, n_2. The default parameters used were R = 25 µm, η = 71°, θ_{in}= 21.4°, n_1=1.37, and n_2=1.27, and one parameter at a time was varied. These results are for θ_{in} and θ_{out} in the index-matched medium are related to the measured angles by Snell's law. **f-h,** Comparison of experimental iridescence maps of index matched Janus droplets with the predicted 3D calculation for (**f**) various sizes, (**g**) illumination angles, and (**h**) droplet morphologies. **f,** Effect of size (radius of curvature) where the contact angle and illumination were fixed at η = 71° and θ_{L} = 30° respectively. **g,** Effect of illumination angle (using the same droplet sample as h(ii)). **h,** Effect of droplet morphology (θ_{L} = 30°). Droplet scale, 50 µm.

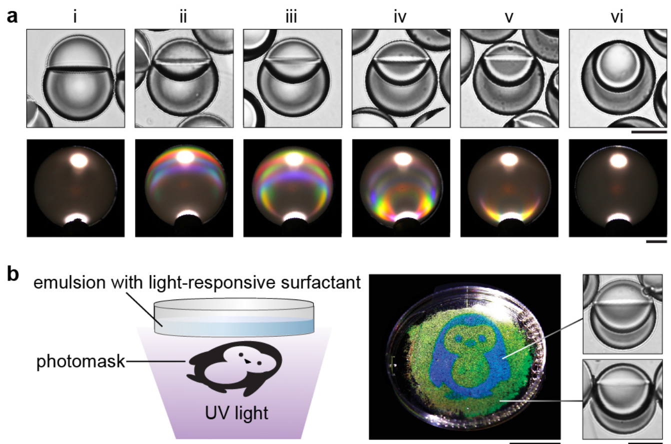

Figure 5 | Iridescence of biphasic oil droplets depends on the curvature of the oil-oil interface. a, Alteration of the internal interfacial curvature in heptane-perfluorohexane biphasic droplets (similar to those shown in Figure 1a) caused a corresponding change in the iridescence. Biphasic droplets with a flat internal interface (far left) and a fully enclosed spherical internal interface (far right) did not display any reflected color. Top row: optical micrographs of example droplets. Scale, 50 µm. Bottom row: photographs of the iridescence pattern as viewed from θ = 0° with an illumination angle of θ = 35°. Scale, 1 cm. **b**, A light responsive surfactant was added to allow photo-patterning of the emulsion shape, and hence, reflected color. Shown is a photograph of a penguin image patterned in droplets in a petri dish (scale, 2 cm) and side view images of the droplet shapes giving rise to the blue and green colors (scale, 50 µm).

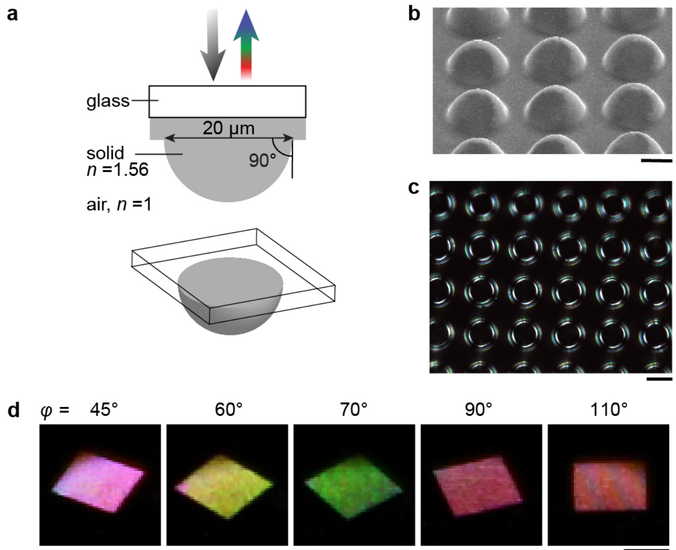

Extended Data Figure 1 | Transparent, polymeric hemispheres printed with multiphoton lithography display iridescence. a, Schematic of the geometry of the hemispheres. **b,** Scanning electron micrograph of the polymeric hemispheres. Scale, 10 µm. **c,** Reflection optical micrograph of the transparent hemispheres. Scale, 20 µm. **d,** Macroscopic DSLR photographs of the hemisphere array as viewed by rotating the camera around the sample under a constant illumination angle. Scale, 1 mm.

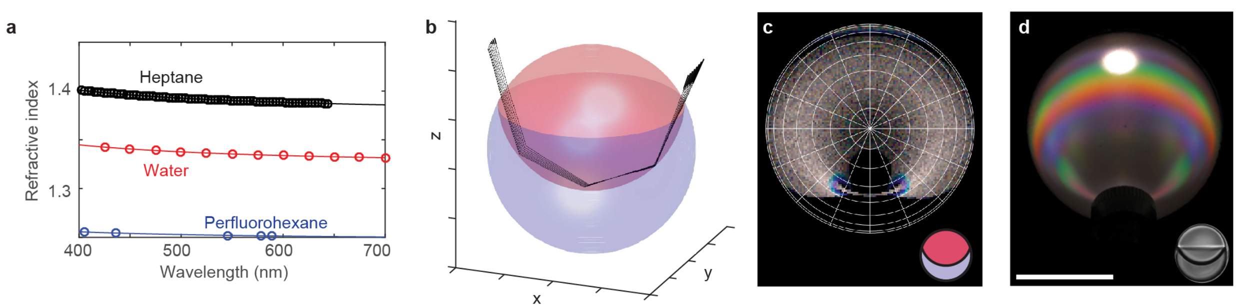

Extended Data Figure 2 | Material dispersion in biphasic droplets does not fully account for the color separation. **a,** Refractive index as a function of wavelength for each of the droplet materials. Water and heptane are both more dispersive than perfluorohexane[27,28]. **b,** Raytracing diagram through the droplet, where the red colored phase is heptane and the grey phase is perfluorohexane. Ray trajectories were determined for a large number of rays, with different refractive index values for each wavelength. Outgoing rays were binned according to angle and wavelength and for each (θ, ϕ) pixel the spectrum was converted to color, yielding **c,** the color separation diagram due to material dispersion. Binning was only necessary for the ray tracer data taking into account the curved upper interface of the droplets. Nothing is binned in the analytical interference model that was used to explain the observed effects. The only color separation is a small amount of blue, where total internal reflection just starts (as the critical angle for blue light is smaller than that of red light). **d,** Experimental iridescent color distribution from a similar droplet geometry for comparison. Scale bar, 20 mm.

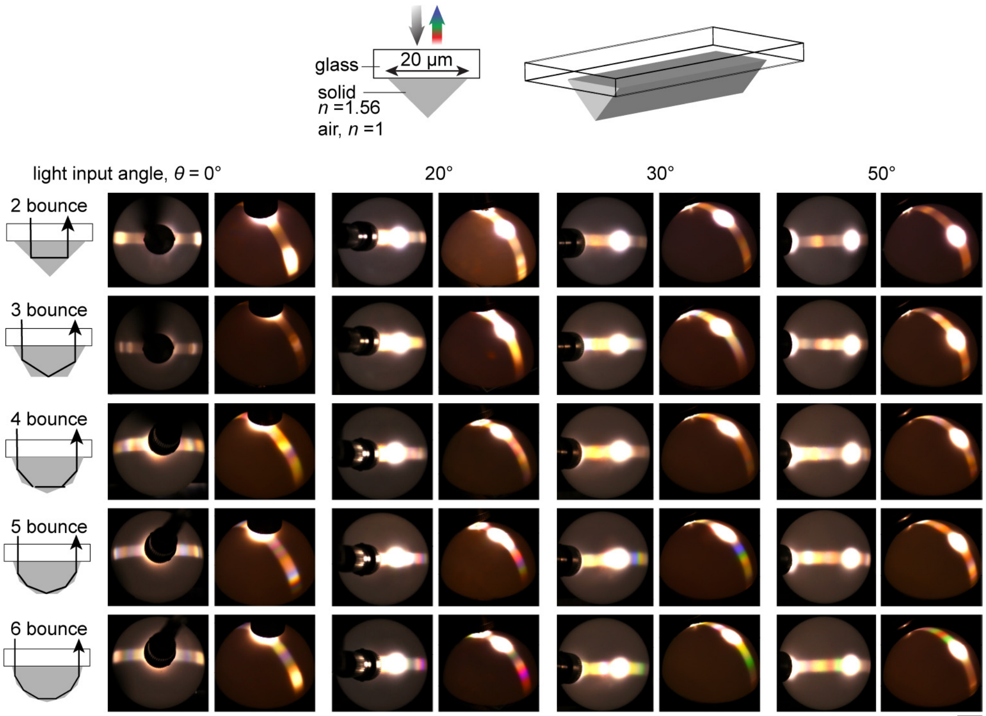

Extended Data Figure 3 | Flat-sided polygonal segments printed with multiphoton lithography display iridescence. The number of sides in the polygon serves to limit the maximum possible number of total internal reflections (diagram at left) that light can undergo for a given illumination angle. Shown are DSLR photographs of the reflected color distributions produced by the same method as described in Figure 2a. The light input direction is provided as θ and the dome was photographed from two viewing angles. Each polygon had a base width of 20 µm. Scale, 1 cm.

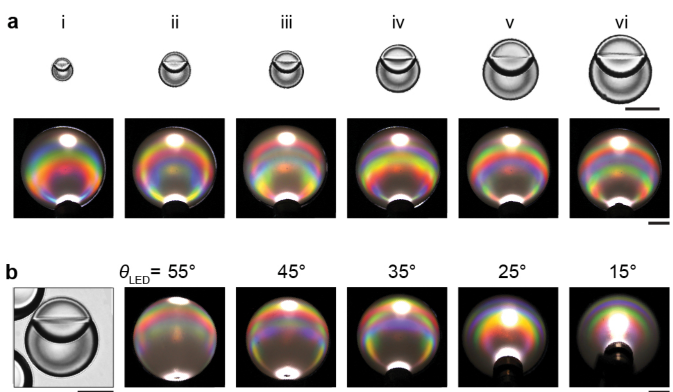

Extended Data Figure 4 | Effect of droplet size and illumination angle on the reflected color distribution from biphasic droplets. a, The iridescence of monodisperse heptane-perfluorohexane droplets with varying diameter but consistent morphology was investigated. Top row: optical micrographs of a droplet from each sample. Scale, 100 µm. Bottom row: photographs of the angular color distribution pattern as viewed from θ = 0° with an illumination angle of θ = 35°. **b**, Far left: optical micrograph of an example biphasic droplet containing heptane and perfluorohexane. Scale, 50 µm. Photographs of the angular color distributions as viewed from θ = 0° when the illumination angle is altered, as shown. Scale, 1 cm.